

A spectral line survey of IRC +10216 between 13.3 and 18.5 GHz

Xiao-Yan Zhang^{1,2}, Qing-Feng Zhu^{1,2}, Juan Li^{3,4}, Xi Chen^{5,3,4}, Jun-Zhi Wang^{3,4}, and Jiang-Shui Zhang⁵

¹ CAS Key Laboratory for Research in Galaxies and Cosmology, Department of Astronomy, University of Science and Technology of China, Hefei 230026, China

e-mail: xyz1128@mail.ustc.edu.cn, zhuqf@ustc.edu.cn

² School of Astronomy and Space Science, University of Science and Technology of China, Hefei 230026, China

³ Department of Radio Science and Technology, Shanghai Astronomical observatory, 80 Nandan RD, Shanghai 200030, China
e-mail: lijuan@shao.ac.cn

⁴ Key Laboratory of Radio Astronomy, Chinese Academy of Sciences, China

⁵ Center for Astrophysics, Guangzhou University, Guangzhou 510006, China

ABSTRACT

A spectral line survey of IRC +10216 between 13.3 and 18.5 GHz is carried out using the Shanghai Tian Ma 65 m Radio Telescope (TMRT-65m) with a sensitivity of < 7 mK. Thirty-five spectral lines of 12 different molecules and radicals are detected in total. Except for SiS, the detected molecules are all carbon-chain molecules, including HC_3N , HC_5N , HC_7N , HC_9N , C_6H , C_6H^- , C_8H , SiC_2 , SiC_4 , $c\text{-C}_3\text{H}_2$ and $l\text{-C}_5\text{H}$. The presence of rich carbon-bearing molecules is consistent with the identity of IRC +10216 as a carbon-rich AGB star. The excitation temperatures and column densities of the observed species are derived by assuming a local thermodynamic equilibrium and homogeneous conditions.

Key words. Stars: individual: IRC+10216 – Radio lines: stars – Line: identification

1. Introduction

IRC+10216 (CW Leo) is a well-known carbon-rich Asymptotic Giant Branch (AGB) star with a high mass-loss rate of about $1^- - 4 \times 10^{-5} M_{\odot} \text{ yr}^{-1}$ (e.g., Crosas & Menten 1997; De Beck et al. 2012; Cernicharo et al. 2015a) at a distance of 123 ± 14 pc (Groenewegen et al. 2012). The effective stellar temperature is between 2500 K and 2800 K (Men'shchikov et al. 2001). The radial velocity (LSR) and terminal expansion velocity of IRC +10216 have been estimated in $-26.5 \pm 0.3 \text{ km s}^{-1}$ and $14.5 \pm 0.2 \text{ km s}^{-1}$, respectively (Cernicharo et al. 2000). IRC+10216 is surrounded by an extended circumstellar envelope (CSE) owing to its extensive mass loss. The CSE is a physically and chemically rich environment to form molecules and condense dust grains (e.g., Fonfría et al. 2008; Agúndez et al. 2012; Fonfría et al. 2014).

Observations at centimeter (cm) and millimeter (mm) wavelengths probe the cool, outer part of AGB winds and bring wealthy evidence of molecular species, from simple radicals such as OH to more complex species like cyanopolynes. In previous works, linear carbon-chain molecules like C_nH , HC_{2n+1}N , and C_nS are observed to be abundant in the circumstellar envelopes of carbon-rich AGB stars (Winnewisser & Walmsley 1978; Cernicharo & Guélin 1996; Guélin et al. 1997; Agúndez et al. 2014; Gong et al. 2015; Agúndez et al. 2017). These molecules are proposed to be related to the formation and destruction of polyaromatic hydrocarbons (PAH) (Henning & Salama 1998; Tielens 2008). The full characterization of carbon-chain molecules is regarded to be an important issue in astrochemistry (Sakai et al. 2010).

Molecular line survey is a powerful tool for analyzing both physical and chemical parameters of astronomical objects. Several systematic spectral line surveys of IRC+10216 have been reported in the literature. From Table 1, we find that existing surveys cover the frequency range from 4 GHz to 636.5 GHz for IRC +10216. Over 80 species (Agúndez et al. 2014) have been discovered toward IRC +10216, including unusual carbon-chain and silicon-carbon molecules such as SiC_2 , MgCCH , NCCP and SiCSi (Thaddeus et al. 1984; Cernicharo et al. 2010; Agúndez et al. 2014; Cernicharo et al. 2015b), metal cyanides/isocyanide such as MgNC , MgCN , AlNC , KCN , FeCN , NaCN , HMgNC and SiH_3CN (Ziurys et al. 1995, 2002; Pulliam et al. 2010; Zack et al. 2011; Agúndez et al. 2012; Cabezas et al. 2013; Agúndez et al. 2014), and even metal halides such as NaCl , KCl , AlCl and AlF (Cernicharo & Guélin 1987; Ziurys et al. 1995; Quintana-Lacaci et al. 2016).

Complex molecules have small rotational constants so that their lowest-energy transitions arise at cm wavelengths. From Table 1, we find that there are several systematic and high sensitivity surveys at cm wavelengths toward IRC +10216. However, no systematic survey has been reported in the frequency range between 6 and 17.8 GHz.

In this paper, the results of a spectral line survey of IRC +10216 between 13.3 and 18.5 GHz are presented. The observations are introduced in Section 2. The observational results derived from the analysis of the molecular emission are shown in Section 3. Section 4 contains the analysis of the lines, the comparison of the results with those of previous works. Finally, the conclusions are presented in Section 5.

Table 1. Existing line surveys of IRC +10216.

Frequencies (GHz)	Telescope	Reference	Sensitivity (1σ) (mJy)	FWHM beam or Angular Resolution ($''$) ^Δ
4–6	Arecibo-305m	Araya et al. (2003)	0.3	46—68
13.3–18.5	TMRT-65m	This work	12	52—73
17.8–26.3	Effelsberg-100m	Gong et al. (2015)	1.0	35—50
28–50	Nobeyama-45m	Kawaguchi et al. (1995)	35	35—62
72–91	Onsala-20m	Johansson et al. (1984, 1985)	665	41—52
80—116		† Agúndez et al. (2014)	23	21—31
129.0—172.5	IRAM-30m	Cernicharo et al. (2000)	78	14—19
197–357.5		Agúndez et al. (2008a)	39	7–13
84.0–115.5	ALMA	Agúndez et al. (2017)	1.3	1.0
131.2–160.3	ARO-12m			39—47
219.5–267.5*	SMT-10m	He et al. (2008)	1400	28—34
214.5—285.5	SMT-10m	Tenenbaum et al. (2010)	140	26—35
253–261	CARMA	Fonfría et al. (2014)	20	0.25
255.3—274.8	ALMA	Cernicharo et al. (2013)	5	0.6
		Velilla Prieto et al. (2015)	17	0.6
293.9–354.8	SMA	Patel et al. (2011)	33	3
330.2—358.1	CSO-10.4m	Groesbeck et al. (1994)	6000	20—22
222.4–267.9°	JCMT-15m	Avery et al. (1992)	3100	18—22
339.6–364.6				15—16
554.5–636.5	Herschel/HIFI	Cernicharo et al. (2010)	3400	33—38

Notes. ^(*) The frequency range from 219.5 GHz to 267.5 GHz was discontinuously covered.

^(°) The frequency range from 222.4 GHz to 267.9 GHz was discontinuously covered.

^(Δ) The FWHM beam sizes are listed for single-dish, the angular resolutions are listed for interferometers.

^(†) There are some other surveys using of IRC +10216 IRAM 30m, although only partially published, e.g., Cernicharo & Guélin (1987, 1996); Guélin et al. (1997, 2000); Ziurys et al. (2002); Guélin et al. (2004); Cernicharo et al. (2007); Agúndez et al. (2007); Cernicharo et al. (2008); Agúndez et al. (2008b); Cernicharo et al. (2011); Agúndez et al. (2012); Cernicharo et al. (2015b).

2. Observations and data reduction

The Tian Ma Radio Telescope (TMRT) is a 65m diameter fully-steerable radio telescope located in the western suburbs of Shanghai, China (Li et al. 2016; Yan et al. 2015). The Digital Backend System (DIBAS) of TMRT is an Field Programmable Gate Array (FPGA) based spectrometer based upon the design of Versatile GBT Astronomical Spectrometer (VEGAS).

The observations were performed in a position-switching mode at Ku band (11.5–18.5 GHz) towards IRC +10216 in 2016 March and April with the TMRT. On-source and off-source integration times were two minutes per scan. In this work, the DIBAS sub-band mode 2 with a single spectral window was adopted for Ku band observation. The window has 16384 channels and a bandwidth of 1500 MHz, supplying a velocity resolution of about 2.08 km s^{-1} (13.3 GHz) to 1.491 km s^{-1} (18.5 GHz). The intensity was calibrated by injecting periodic noise, and the accuracy of the calibration was estimated from frequency ranges where the spectrum was apparently free of lines. The system temperature was about 55 – 64 K at Ku band. Across the whole frequency range, the FWHM beam size was $52''$ – $84''$. The adopted coordinates for our searches were: R.A. (2000) = 09:47:57.45, DEC (2000) = 13:16:43.8. The pointing accuracy was better than $12''$. The resulting antenna temperatures were scaled to main beam temperatures (T_{MB}) by using a main beam efficiency of 0.6 for a moving position of sub-reflector at Ku band (Li et al. 2016).

The data were reduced using GILDAS software package¹ including CLASS and GREG. Linear baseline subtractions were used for all the spectra. Because of the contamination due to time variable radio frequency interference (RFI), the channels from 11.5 GHz to 13.3 GHz were discarded from further analysis. Since some unknown defects occurred at the edges of the spectra, the channels with a bandwidth of 150 MHz at each edge were excluded. All the spectra including two polarizations were averaged to reduce rms noise levels.

3. Results

Based on the molecular database “Splatalogue”², which is a compilation of the Jet Propulsion Laboratory (JPL, Pickett et al. 1998), Cologne Database for Molecular Spectroscopy catalogues (CDMS, Müller et al. 2005), and Lovas/NIST catalogues (Lovas 2004), the line identifications are performed. The local standard of rest (LSR) radial velocity of -26.5 km s^{-1} is adopted to derive the rest frequency of the observed lines. A line is considered real if it has a signal-to-noise ratio (S/N) of at least five (Gong et al. 2015), although, a line is already significant if it is characterized by a S/N above three (Fonfría et al. 2014). Lines with a S/N of at least three are discussed in this paper. Figure 1 presents an overview of the spectral line survey of IRC +10216 between 13.3 and 18.5 GHz with strong lines marked.

¹ <http://www.iram.fr/IRAMFR/GILDAS>.

² www.splatalogue.net.

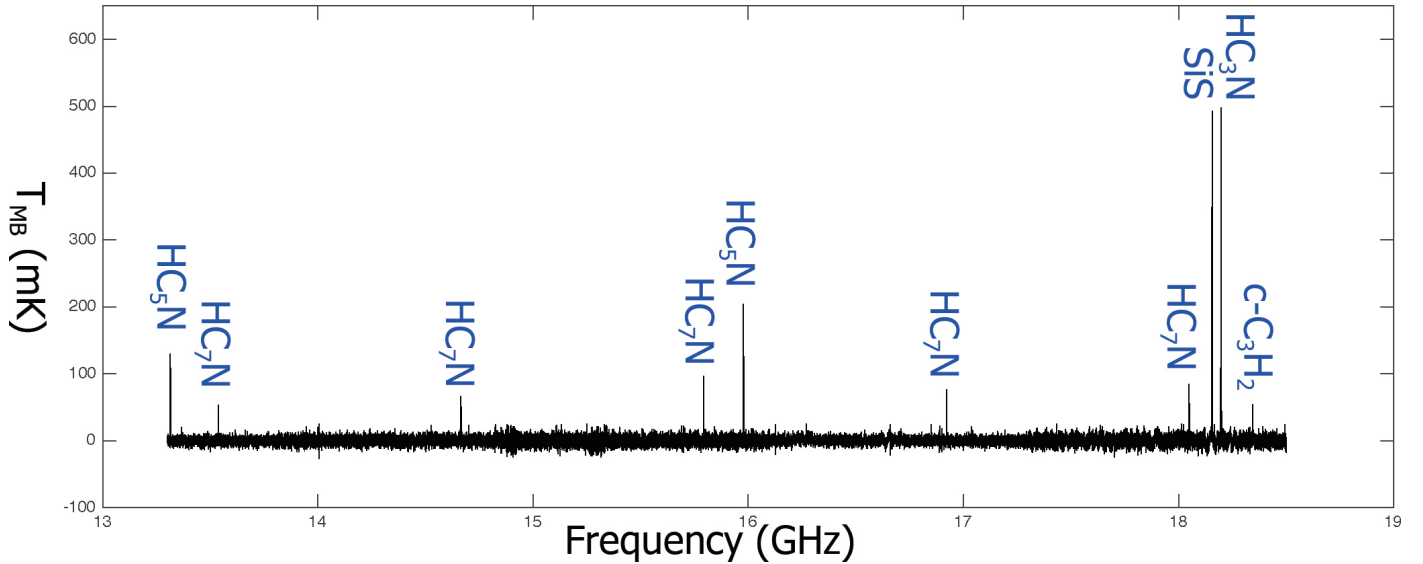


Fig. 1. Overview of the spectral line survey of IRC +10216 between 13.3 and 18.5 GHz with strong lines marked.

All detected transitions are shown in Figure 2 and Table 2. There are 41 transitions assigned to 12 different molecules and radicals found in this survey. Except for SiS, all other molecules are C-bearing molecules. The detected transitions include one transition of HC₃N, three transitions of the ¹³C-bearing isotopologues of HC₃N, two transitions of HC₅N, five transitions of HC₇N, and nine transitions of HC₉N, which are shown in Figure 2(a) and Figure 2(b). In Figure 2(a), HC¹³CCN ($\nu = 0, J = 2 - 1$) is blended with HCC¹³CN ($\nu = 0, J = 2 - 1$). Additionally, eight transitions of C₆H are detected. In Figure 2(c), C₆H ($^2\Pi_{3/2}, J = 11/2 - 9/2, l = f$) is blended with C₆H ($^2\Pi_{3/2}, J = 11/2 - 9/2, l = e$), and C₆H ($^2\Pi_{3/2}, J = 13/2 - 11/2, l = f$) is blended with C₆H ($^2\Pi_{3/2}, J = 13/2 - 11/2, l = e$). There is a transition of c-C₃H₂, five transitions of l-C₅H from the $^2\Pi_{1/2}$ ladder and one transition of C₆H⁻ in Figure 2(c). Spectra line profiles of three transitions of C₈H from the $^2\Pi_{3/2}$ ladder, SiS ($\nu = 0, J = 1 - 0$), SiC₂ ($\nu = 0, J = 7(2,5) - 7(2,6)$) and SiC₄ ($\nu = 0, J = 5 - 4$) are shown in Figure 2(d). There are five transitions of SiC₂ and two transitions of SiC₄ in this band. But other transitions of SiC₂ and SiC₄ are too weak to be detected. The peak intensities of the smoothed lines of HC¹³CCN, HCC¹³CN, l-C₅H, C₈H $^2\Pi_{3/2}$ and C₆H $^2\Pi_{1/2}$ are smaller than 20 mK. These smoothed lines are weak and tentatively detected. The rest frequencies and the upper energy levels of these lines are obtained from the molecular database “Splatologue”.

The SHELL fitting routine in Continuum and Line Analysis Single-dish Software (CLASS) is used to derive line parameters including peak intensity, integrated intensity, and expansion velocity which is defined as the half-width at zero power. Except for the blended lines, the observed lines are either double peaked or flat-topped. The fitting profiles are shown in Figure 2 when possible. For the line of HC₃N with hyperfine structure, only the main component is fitted to obtain the expansion velocity. For the lines that are blended and weak, the parameters are estimated directly by integrating the line profiles. Firstly, estimate the maximum velocities ν_1 and ν_2 of blueshift and redshift. Then, return the integrated area (K km/s) of the current spectrum between velocities ν_1 and ν_2 by using the function TDV(ν_1, ν_2) in CLASS. The observed properties of the lines are displayed in Table 2.

The spectrum is dominated by the strong transitions from five species: SiS, HC₃N, HC₅N, HC₇N and c-C₃H₂. The peak intensities of SiS, HC₃N and HC₅N lines are larger than 120 mK. The peak intensities of HC₇N and c-C₃H₂ lines are larger than 50 mK. The peak intensities of other lines are about 20 mK. Weak lines with the peak intensities smaller than 20 mK have been smoothed to have a channel width of 3.0 – 3.6 km s⁻¹ to improve signal to noise ratios. The smoothed lines are marked with red “smoothed” in the upper left of the corresponding panels in Figure 2 and marked with “S” in Table 2. The rms noise of peak intensity, which is estimated by fitting the baseline to a line or polynomial from frequency ranges around each particular transition where the spectrum is apparently free of lines, is about 3 – 7 mK in 1.5 – 3.6 km s⁻¹ wide channel. Since the terminal expansion velocity of IRC +10216 have been estimated in ~ 14.5 km s⁻¹ in previous studies. The error of integrated intensity given in this work, which is the product of the rms noise of peak intensity and the width of the line for about 29 km s⁻¹, is about 100 – 200 mK km s⁻¹. The lines in this work reveal an average LSR velocity of about -26.7 ± 2.0 km s⁻¹ and an average terminal expansion velocity of about 13.9 ± 2.0 km s⁻¹, which are consistent with previous studies (e.g., -26.5 ± 0.3 km s⁻¹ and 14.5 ± 0.2 km s⁻¹, respectively (Cernicharo et al. 2000), -26.404 ± 0.004 km s⁻¹ and 13.61 ± 0.05 km s⁻¹, respectively (He et al. 2008)).

4. Discussion

It was suggested that single-peaked lines arise from optically thick transitions, while flat-topped and double-peaked lines arise from optically thin spatially unresolved and resolved transitions, respectively (Olofsson et al. 1982; Kahane et al. 1988). There are 11 double peaked lines and 19 flat-topped lines among the 30 unblended lines detected in this work. Therefore, we can assume optically thin for the lines detected in this work. By assuming LTE, rotational temperatures and column densities can be estimated from the

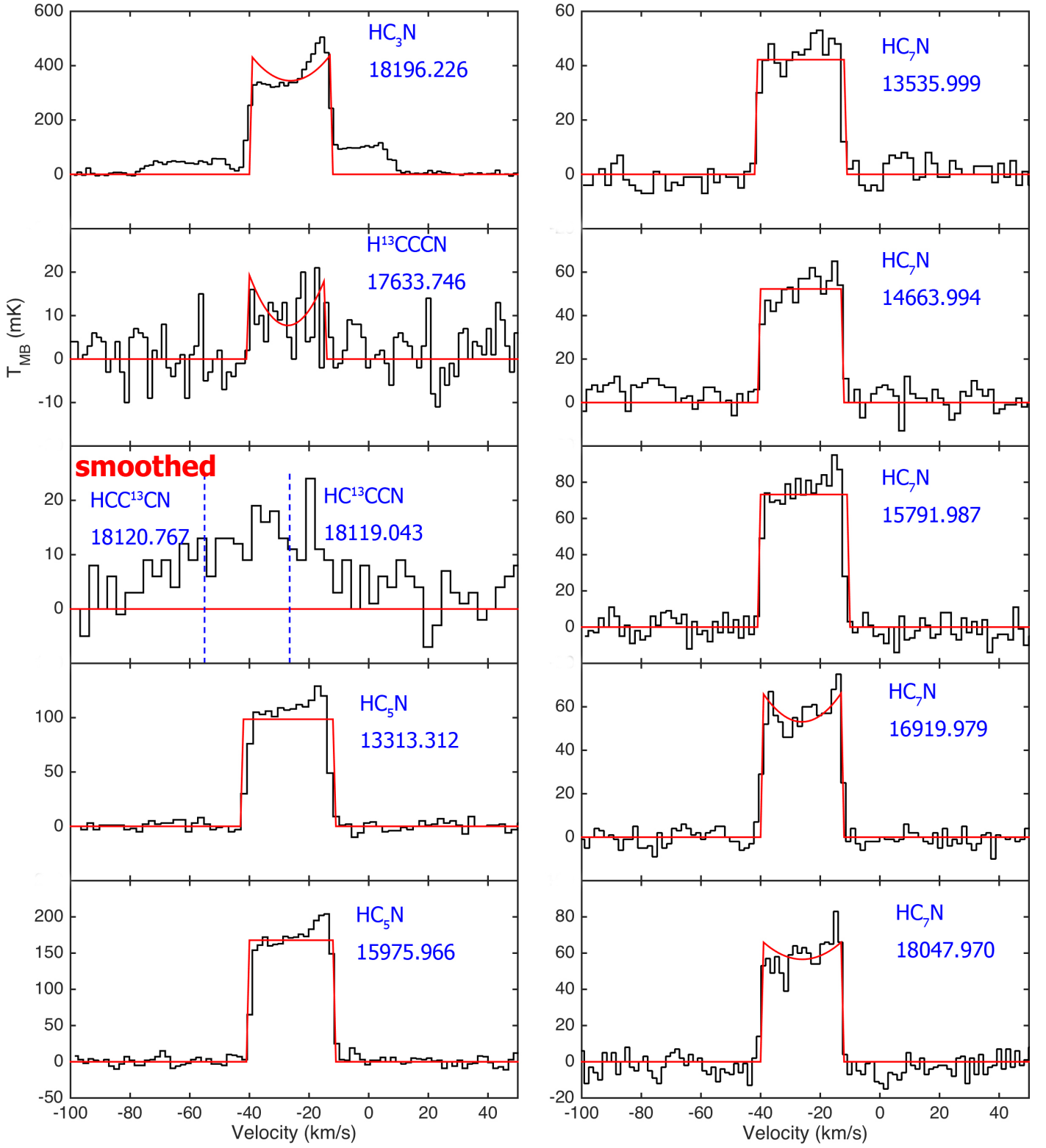


Fig. 2. (a) Zoom in of all detected and tentatively detected lines for HC_3N , H^{13}CCCN , HC^{13}CCN , HCC^{13}CN , HC_5N and HC_7N . The corresponding rest frequency in MHz are shown in the upper right of each panel. Weak lines have been smoothed to have a channel width of $3.0\text{--}3.6\text{ km s}^{-1}$, and are marked with “smoothed” in the upper left of the corresponding panels. Otherwise, the channel width is $1.5\text{--}2.1\text{ km s}^{-1}$. The blue dashed lines of the blended transitions trace the systematic LSR velocity (-26.5 km s^{-1}) of IRC +10216.

rotational diagrams. The equation (Cummins et al. 1986):

$$N = \frac{3kW}{8\pi^3\nu S\mu^2} Q(T_{rot}) \frac{T_{rot}}{T_{rot} - T_{bg}} \exp(E_U/kT_{rot}) \quad (1)$$

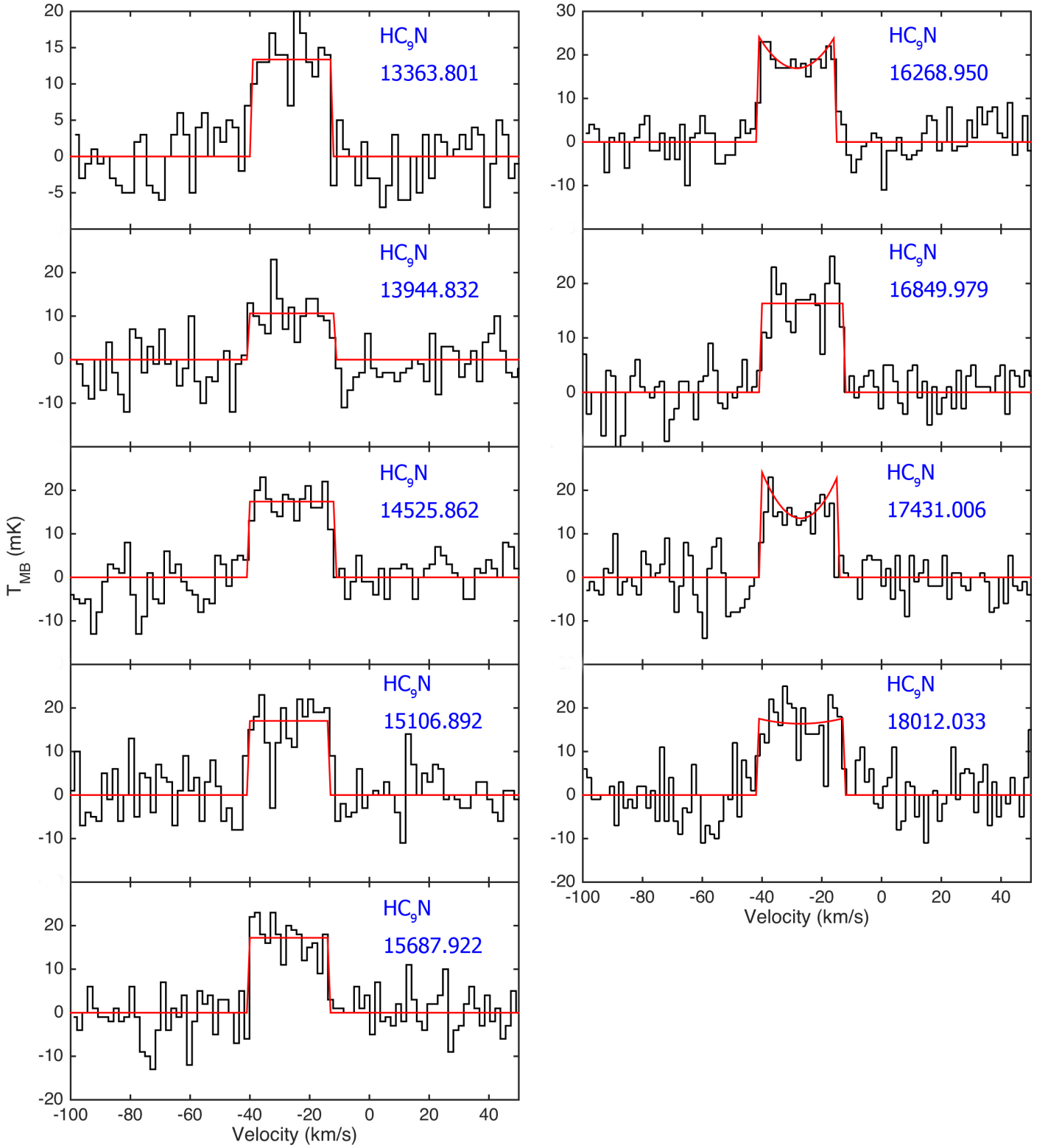


Fig. 2. (b) Same as Fig.2.(a) for HC₉H.

gives the relation between the column density and the line intensity, where k is the Boltzmann constant, W ($\int T_R dV$, K km s^{-1}) is the observed line integrated intensity, ν (Hz) is the frequency of the transition, $S\mu^2$ is the product of the total torsion-rotational line strength and the square of the electric dipole moment. T_{rot} and T_{bg} (2.73 K) are the rotational temperature and background brightness temperature, respectively. E_u is the upper level energy, and $Q(T_{rot})$ is the partition function. Values of E_U/k and $S\mu^2$ are taken from the ‘‘Splatalogue’’ spectral line catalogs.

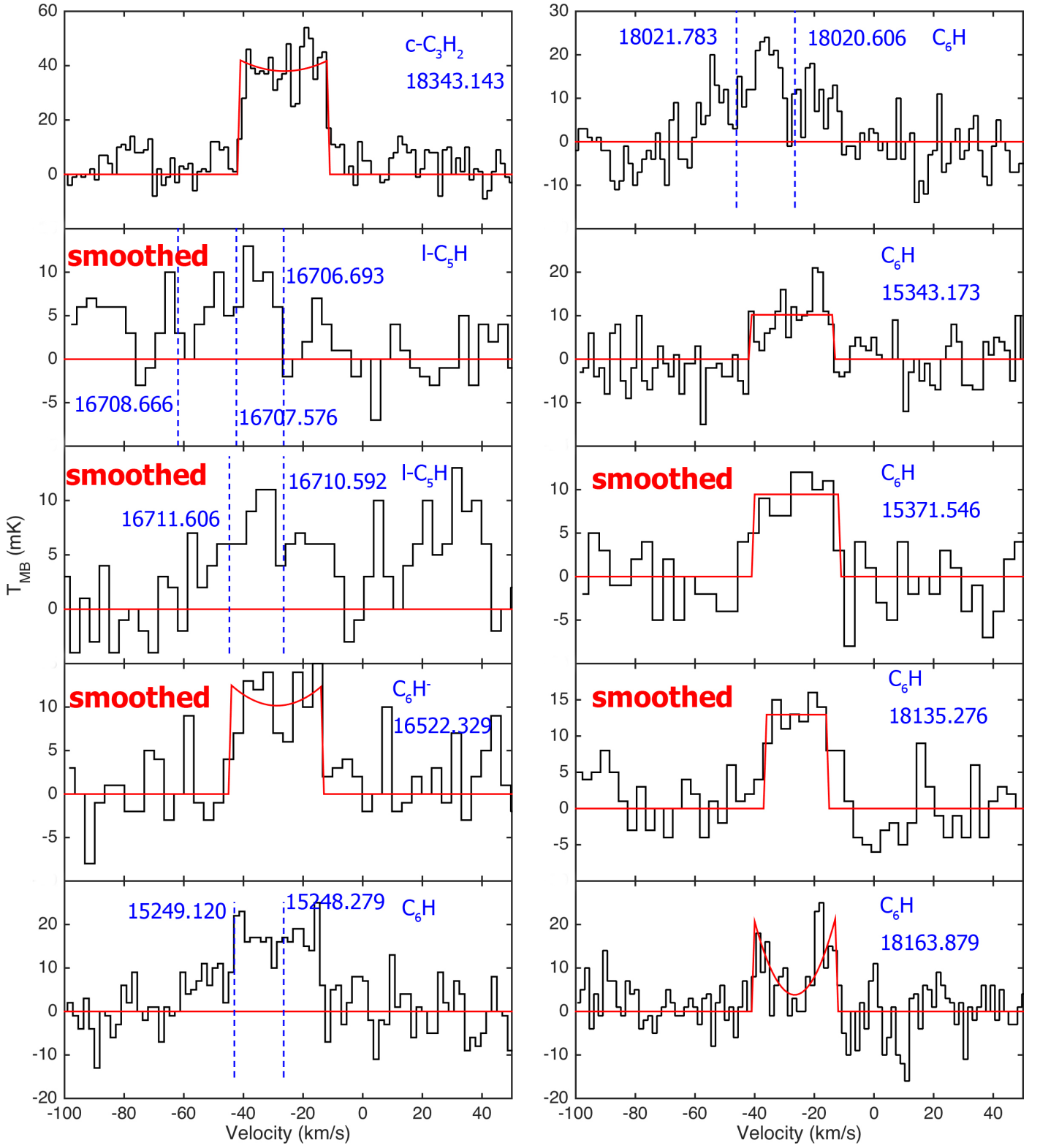


Fig. 2. (c) Same as Fig.2.(a) for C_nH

From equation (1), the formula for rotational diagrams is:

$$\ln \frac{3kW}{8\pi^3\nu S\mu^2} = \ln \frac{N}{Q(T_{rot}^*)} - \frac{E_U}{kT_{rot}} \quad (2)$$

where $Q(T_{rot}^*) = Q(T_{rot}) \frac{T_{rot}}{T_{rot} - T_{bg}}$. To determine rotational temperatures with this method, there must be at least two transitions of the same molecule with significant rotational temperature differences.

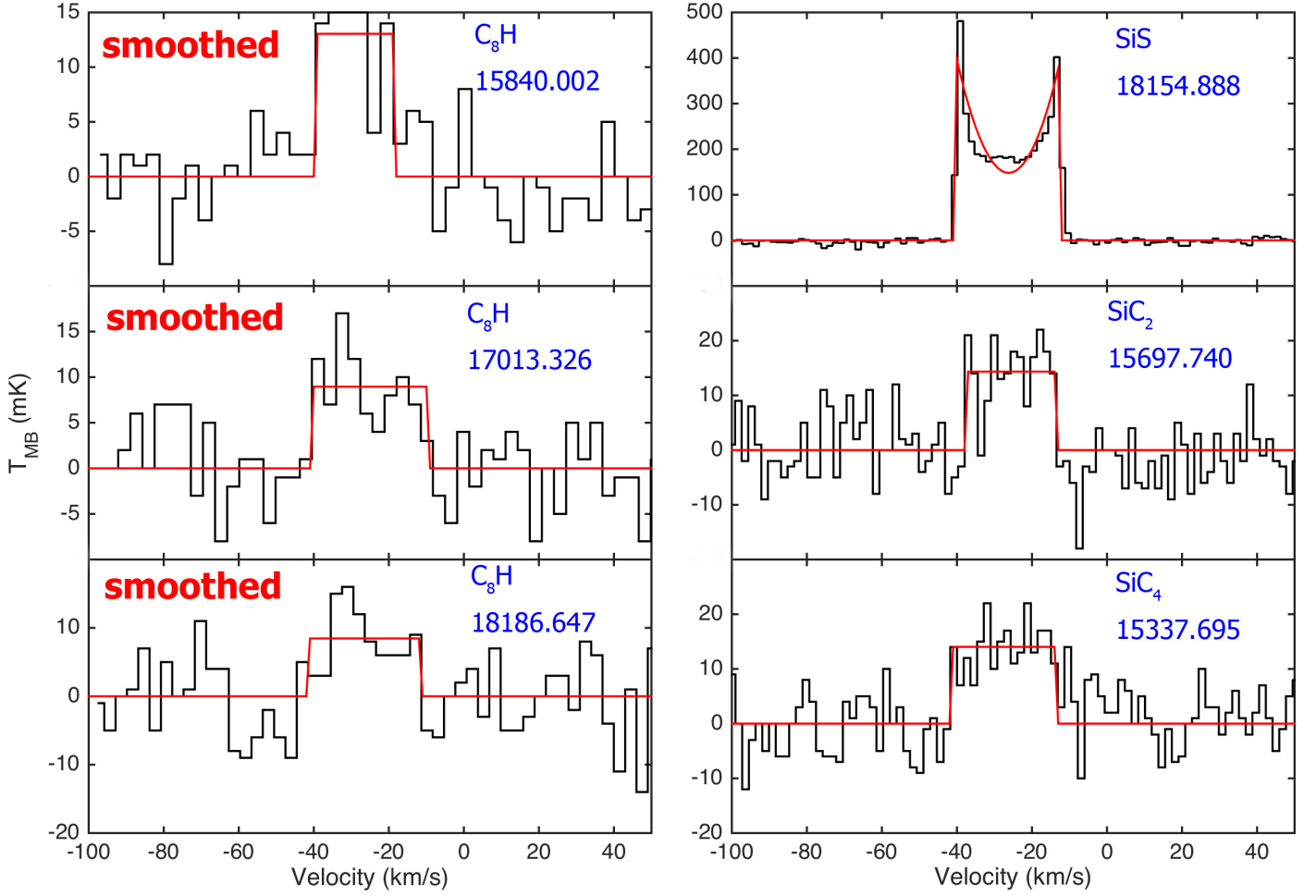


Fig. 2. (d) Same as Fig.2.(a) for C_8H and Si bearing species.

$SiS(1-0)$ is a maser in IRC +10216 (Henkel et al. 1983) and its populations must deviate from LTE, therefore this transition is excluded from the fitting. The lines of $HC^{13}CCN(v=0, J=2-1)$ and $HCC^{13}CN(v=0, J=2-1)$ are blended owing to large uncertainties of intensities, so are also excluded. Since only one line is detected in this work for each of HC_3N , $H^{13}CCCN$, $c-C_3H_2$, SiC_2 , SiC_4 and C_6H^- , these lines can not be used to determine rotational temperatures directly. For molecules of HC_5N , HC_7N , HC_9N , C_6H , C_8H and $l-C_5H$, although at least two lines are detected, they do not have a wide dynamic range in upper level energies. The 17.8 GHz to 26.3 GHz data from Gong et al. (2015), the 28 GHz to 50 GHz data from Kawaguchi et al. (1995), the C_8H data from Remijan et al. (2007) and the $H^{13}CCCN$ data from He et al. (2008) are adapted as the complementary to data in the current survey to derive rotational temperatures more precisely.

The integrated intensity ($\int T_{MB} dv$, $mK km s^{-1}$) of Gong et al. (2015) is obtained from the integrated flux density ($\int S_\nu dv$, $mJy km s^{-1}$), which is taken from Table 3 in Gong et al. (2015). And the conversion factor from the flux density (S_ν , Jy) to the main beam brightness temperature (T_{mb} , K) is $T_{mb}/S_\nu \sim 1.5 K/Jy$ at 22 GHz. In Gong et al. (2015), across the whole frequency range, the beam size is $35'' - 50''$ ($\sim 40''$ at 23 GHz). The rms noise of intensity is estimated in the same way as in this work using online-data of the observed spectrum. In Kawaguchi et al. (1995), the main beam efficiency (η) was measured to be 0.78 ± 0.06 at 30 GHz, 0.79 ± 0.05 at 43 GHz and 0.71 ± 0.07 at 49 GHz. The main beam efficiency at the other frequencies was assumed to be 0.78 in the region between 28 and 35 GHz, and was interpolated from the measured values in the region between 35 and 50 GHz. The measured beam size (FWHM) was $34.9'' \pm 1.1''$ at 49 GHz and $41.5'' \pm 1.1''$ at 43 GHz. The brightness temperature (T_R) of the molecular transition in the source is related to the antenna temperature (T_A^*) as $T_R = T_A^*/(\eta \eta_{BD})$. The integrated intensity ($\int T_A^* dv$) and the rms noise of antenna temperature are taken from Table 1 in Kawaguchi et al. (1995). In Remijan et al. (2007), the beam size (FWHM) is approximated by $\theta_{beam} = 740''/\nu(GHz)$. The main beam efficiency (η), the integrated intensity ($\int T_A^* dv$) and the error to the integrated intensity are taken from Table 1 in Remijan et al. (2007). In He et al. (2008), the FWHM beam size of the KP12M is $43''$ at 145 GHz. The integrated intensity ($\int T_{MB} dv$) and the rms noise of main beam temperature are taken from Table 10 in He et al. (2008). The errors to the integrated intensities of Gong et al. (2015), He et al. (2008) and Kawaguchi et al. (1995) are computed in the same way with this work.

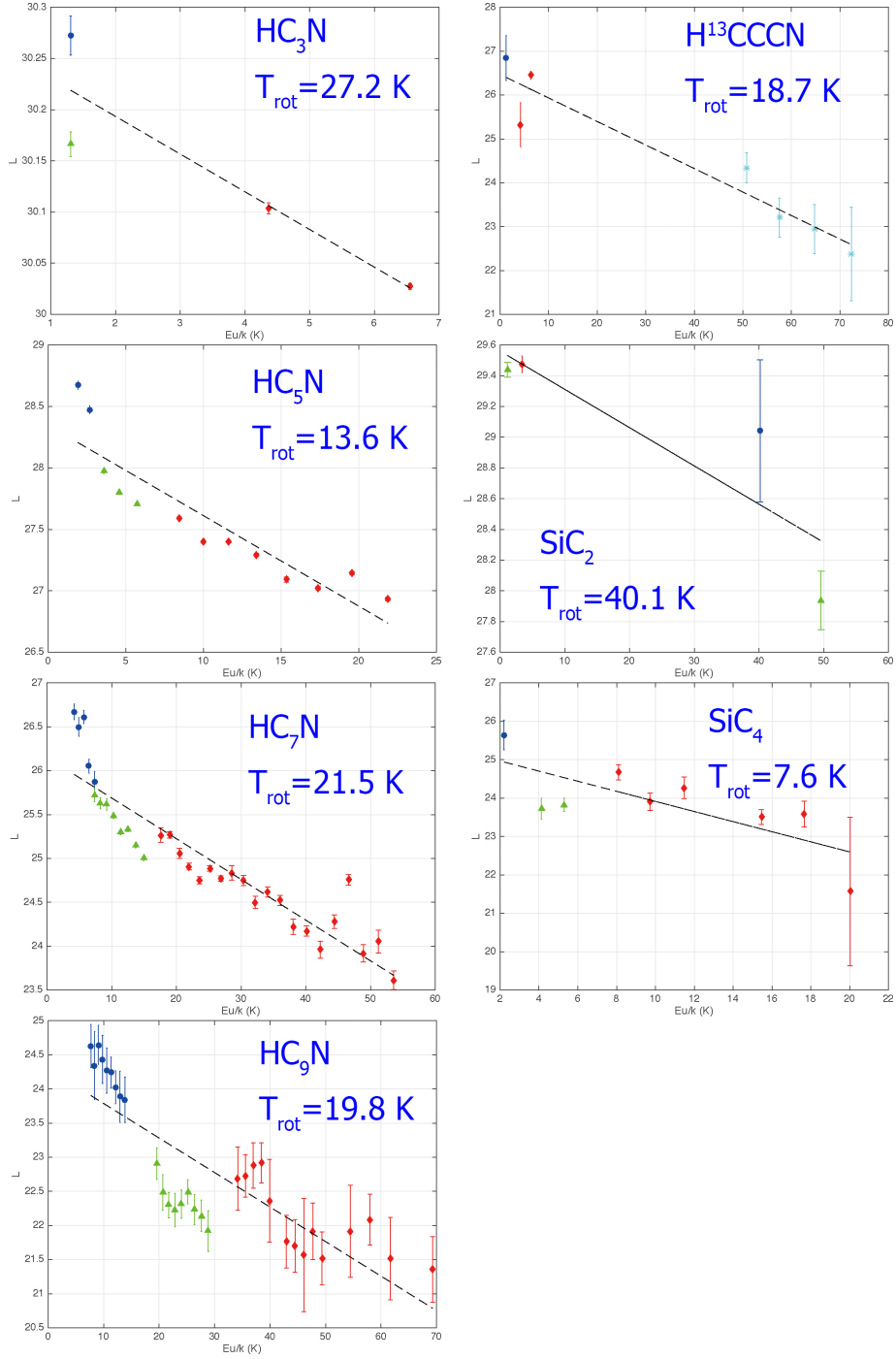


Fig. 3. Rotational diagrams for the observed molecules in IRC +10216. The variable L denotes the left-hand side of equation (2). Black dashed lines represent linear least-squares fit to the rotational diagram. The blue circles are from our TMRT-65 m observations. The green triangles are obtained from Gong et al. (2015). The red diamonds are obtained from Kawaguchi et al. (1995). The magenta crosses are obtained from Remijan et al. (2007). The cyan asterisks are obtained from He et al. (2008). Their values have been corrected for beam dilution. The molecules and their corresponding rotational temperatures are given in each panel.

The intensities of the detected lines should be divided by $\theta_s^2/(\theta_s^2 + \theta_{beam}^2)$ for beam dilution to derive the physical parameters, where θ_s is the source size, and θ_{beam} is the beam size (Bell 1993). So, the brightness temperature (T_R) of the molecular transition in the source is related to the main beam temperature (T_{MB}) as

$$T_R = T_{MB}/\eta_{BD} = T_{MB} \frac{\theta_{beam}^2 + \theta_s^2}{\theta_s^2} \quad (3)$$

The source sizes are taken based on previous high resolution mapping of different molecules toward IRC +10216 by interferometer. For species without high resolution mapping, their sizes are taken to be the same as chemically related species. Therefore,

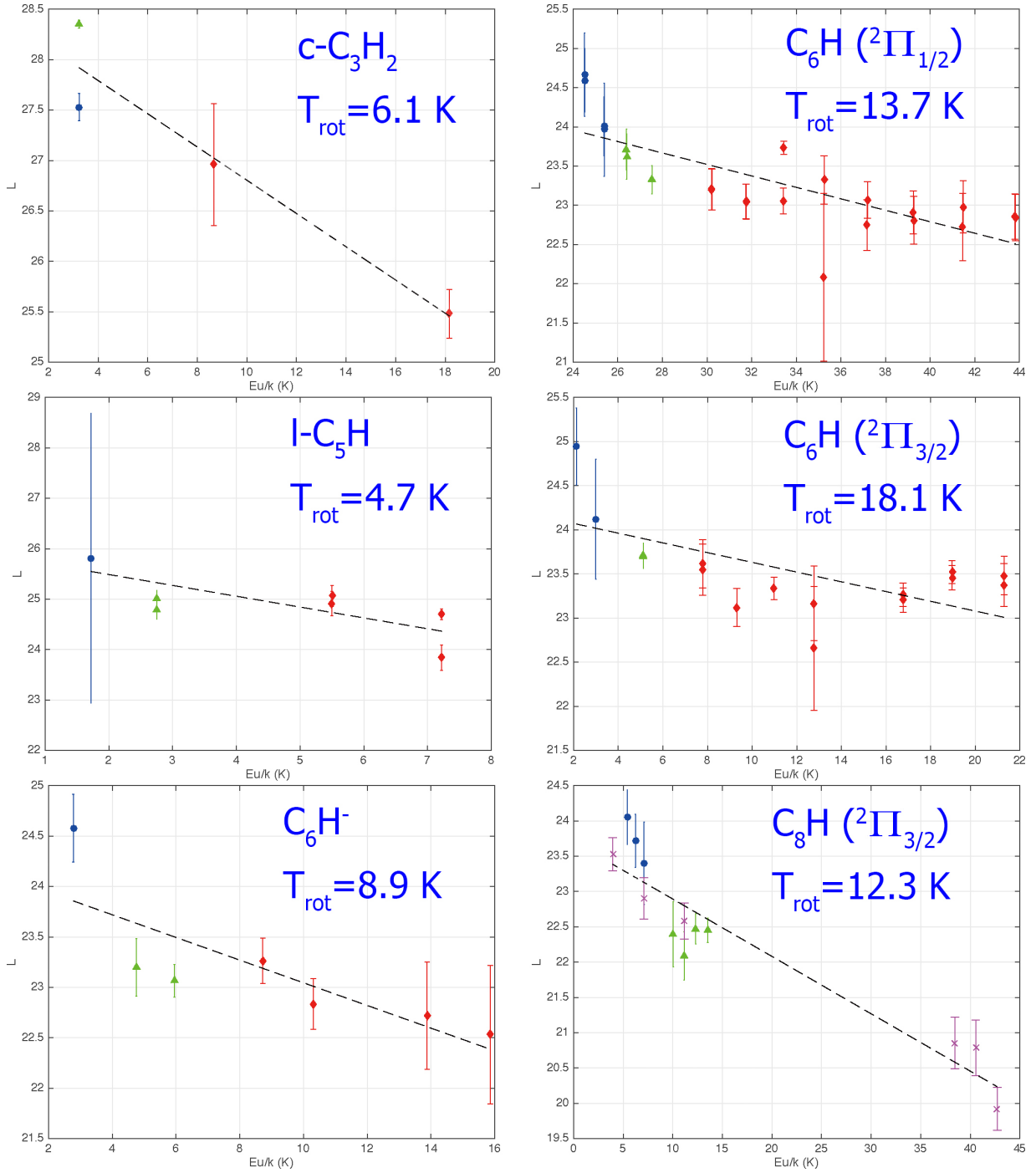


Fig. 3. continued.

source sizes of HC_3N and HC_5N are $30''$ that determined by new JVLA observations. Source size of H^{13}CCCN is taken to be the same as that of HC_3N . Source sizes of HC_7N and HC_9N are taken to be the same as that of HC_5N . The sizes of $\text{I-C}_5\text{H}$, $c\text{-C}_3\text{H}_2$, C_6H , C_6H^- and C_8H are taken to be the same as that of C_4H (Guélin et al. 1993), which is $30''$. The size of SiC_2 is $27''$, and the source size of SiC_4 is assumed to be the same as it (Lucas et al. 1995). The size of SiS is $18''$ by IRAM Plateau de Bure interferometer (Lucas et al. 1995). We carried out linear least-square fits to the rotational diagrams of 12 species. The results are shown in Figure 3 and Table 3. The results of Gong et al. (2015) and Kawaguchi et al. (1995) in Table 3 are obtained from the methods of rotational diagrams as well.

This work assumes the same source sizes as Gong et al. (2015), and the H_2 average column density (N_{H_2}) of $2.1 \times 10^{21} \text{ cm}^{-2}$ within a typical radius of $15''$ taken from Gong et al. (2015) is used to calculate molecular fractional abundances relative to H_2 . The derived rotational temperatures (T_{rot}), column densities (N) and molecular fractional abundances relative to H_2 ($X(N/N_{\text{H}_2})$) together with results from the literature, are listed in Table 3. The column densities of the molecules range from 10^{12} to 10^{15} cm^{-2} , and the fractional abundances relative to H_2 of the species detected in Ku band range from 2.91×10^{-9} to 9.24×10^{-7} in IRC +10216.

Table 3. Column densities and rotational temperatures of the molecules in IRC +10216.

Species	$T_{rot}(K)$	$N \text{ cm}^{-2}$	$X(N/N_{H_2})$	Ref.
HC ₃ N	27.2 ± 19.4	$(1.94 \pm 0.21) \times 10^{15}$	9.24×10^{-7}	0
	24.7 ± 18.5	$(1.4 \pm 0.2) \times 10^{15}$	6.7×10^{-7}	1
	26	1.7×10^{15}		2
H ¹³ CCCN	18.7 ± 3.3	$(3.25 \pm 1.46) \times 10^{13}$	1.55×10^{-8}	0
HC ₅ N	13.6 ± 2.1	$(5.47 \pm 0.77) \times 10^{14}$	2.61×10^{-7}	0
	18.8 ± 1.3	$(4.6 \pm 0.2) \times 10^{14}$	2.2×10^{-7}	1
	27 ± 5	$(2.7 \pm 0.2) \times 10^{14}$		2
HC ₇ N	21.5 ± 1.7	$(6.21 \pm 0.67) \times 10^{14}$	2.96×10^{-7}	0
	12.1 ± 1.3	$(3.7 \pm 0.4) \times 10^{14}$	1.8×10^{-7}	1
	26 ± 2	$(1.52 \pm 0.07) \times 10^{14}$		2
HC ₉ N	19.8 ± 2.4	$(5.88 \pm 1.28) \times 10^{13}$	2.80×10^{-8}	0
	20.9 ± 10.7	$(2.5 \pm 1.4) \times 10^{13}$	1.2×10^{-8}	1
	23 ± 8	$(2.7 \pm 0.9) \times 10^{13}$		2
c-C ₃ H ₂	6.1 ± 2.8	$(1.39 \pm 1.07) \times 10^{14}$	6.60×10^{-8}	0
	5.5 ± 0.6	$(2.1 \pm 0.4) \times 10^{14}$	9.9×10^{-8}	1
l-C ₅ H ² Π _{1/2}	4.7 ± 2.0	$(2.96 \pm 1.21) \times 10^{14}$	1.41×10^{-7}	0
	8.3 ± 2.0	$(2.9 \pm 0.6) \times 10^{13}$	1.4×10^{-8}	1
	27 ± 5	$(2.9 \pm 0.3) \times 10^{14}$		2
C ₆ H ⁻	8.9 ± 3.4	$(6.11 \pm 2.99) \times 10^{12}$	2.91×10^{-9}	0
	26.9 ± 4.0	$(5.8 \pm 0.5) \times 10^{12}$	2.8×10^{-9}	1
C ₆ H ² Π _{1/2}	13.7 ± 2.7	$(1.85 \pm 0.90) \times 10^{14}$	8.82×10^{-8}	0
	20.7 ± 2.4	$(1.0 \pm 0.2) \times 10^{14}$	4.8×10^{-8}	1
	46 ± 4	$(1.13 \pm 0.6) \times 10^{14}$		2
C ₆ H ² Π _{3/2}	18.1 ± 5.8	$(5.38 \pm 1.18) \times 10^{13}$	2.56×10^{-8}	0
	47.2 ± 10.3	$(1.0 \pm 0.1) \times 10^{14}$	4.8×10^{-8}	1
	35 ± 2	$(1.65 \pm 0.07) \times 10^{14}$		2
C ₈ H ² Π _{3/2}	12.3 ± 1.6	$(5.00 \pm 1.08) \times 10^{13}$	2.38×10^{-8}	0
	13.9 ± 1.3	$(8.4 \pm 1.4) \times 10^{12}$	4.0×10^{-9}	1
SiC ₂	40.1 ± 36.2	$(1.87 \pm 1.34) \times 10^{15}$	8.90×10^{-7}	0
	31.8 ± 0.9	$(1.2 \pm 0.0) \times 10^{15}$	5.7×10^{-7}	1
	16	2.2×10^{14}		2
SiC ₄	7.6 ± 3.0	$(1.46 \pm 0.92) \times 10^{13}$	6.98×10^{-9}	0
	22.3 ± 17.5	$(1.1 \pm 0.4) \times 10^{13}$	5.2×10^{-9}	1

Notes. References for rotational temperatures and column densities from : (0) This work; (1) Gong et al. (2015); (2) Kawaguchi et al. (1995). The results of Gong et al. (2015) and Kawaguchi et al. (1995) are also used the method of rotational diagrams.

The blue-shifted component of the SiS ($v = 0, J = 1 - 0$) line shown in Figure 2(d) is stronger than the red-shifted one due to maser amplification (18154.9 MHz; Henkel et al. 1983). The peak intensity ratio of the blue-shifted component to the red-shifted component is estimated to be 1.97 ± 0.02 in Gong et al. (2015). In this work, the peak intensity ratio is about 1.20 ± 0.02 , which is smaller than the ratio observed in Gong et al. (2015). The reason for the difference of the peak intensity ratio of SiS may be that the velocity resolution at 18154.888 MHz of 1.5 km s^{-1} in the work is bigger than that of 1.008 km s^{-1} in Gong et al. (2015). Lines of HC₇N ($v = 0, J = 16 - 15$), HC₃N ($v = 0, J = 2 - 1$) and c-C₃H₂ ($v = 0, J = 1(1, 0) - 1(0, 1)$) have also been detected in Gong et al. (2015). The parameters of HC₇N ($v = 0, J = 16 - 15$), SiS ($v = 0, J = 1 - 0$), HC₃N ($v = 0, J = 2 - 1$) and c-C₃H₂ ($v = 0, J = 1(1, 0) - 1(0, 1)$) in this work are shown in Table 2. The observed properties of these lines are displayed in Table 4.

The integrated intensities ($\int T_R dv$) are shown in Table 5. The integrated intensities of HC₇N ($v = 0, J = 16 - 15$), SiS ($v = 0, J = 1 - 0$) and HC₃N ($v = 0, J = 2 - 1$) in this work are consistent with the results derived from Gong et al. (2015). But the integrated intensity of c-C₃H₂ ($v = 0, J = 1(1, 0) - 1(0, 1)$) in this work is much smaller than that in Gong et al. (2015). Since the c-C₃H₂ ($v = 0, J = 1(1, 0) - 1(0, 1)$) line is at the edge of frequency range covered by the receiver, the flux calibration is less reliable there.

Light variability may also affect the accuracy of the integrated intensities. Intensity comparisons are more difficult for weaker lines. And for abundant species and their isotopologues toward the archetypical circumstellar envelope of IRC+10216, based on the existed observations (Cernicharo et al. 2000, 2014), some line intensities of the high rotational lines may follow the infrared flux variations, and some line intensities of the low-J transitions may not. But there is no direct evidence indicating line intensities of the emission lines detected in this work, Gong et al. (2015) and Kawaguchi et al. (1995) correlate with the continuum intensity. Since most of the detected lines in this work are weak, and the data for the strong transitions in this work is not enough to study the

Table 4. Line Parameters of HC₇N ($\nu = 0, J = 16 - 15$), SiS ($\nu = 0, J = 1 - 0$), HC₃N ($\nu = 0, J = 2 - 1$) and c-C₃H₂ ($\nu = 0, J = 1(1, 0) - 1(0, 1)$) detected by This work and Gong et al. (2015).

Species	Transitions	Rest Freq. (MHz)	$\int T_{MB} d\nu$ (mK km s ⁻¹)		θ_s (")	θ_{beam} (")	
			This Work	Gong		This Work	Gong
HC ₇ N	$\nu = 0, J = 16 - 15$	18047.970	1629(194)	1577(116)	30	54	50
SiS	$\nu = 0, J = 1 - 0$	18154.888	6692(186)	7140(110)	18	53	49
HC ₃ N	$\nu = 0, J = 2 - 1$	18196.226	10337(197)	10445(125)	30	53	49
c-C ₃ H ₂	$\nu = 0, J = 1(1, 0) - 1(0, 1)$	18343.143	1161(157)	2973(116)	30	53	49

Table 5. The integrated intensity ratios (This Work: Gong et al. (2015)) of HC₇N ($\nu = 0, J = 16 - 15$), SiS ($\nu = 0, J = 1 - 0$), HC₃N ($\nu = 0, J = 2 - 1$) and c-C₃H₂ ($\nu = 0, J = 1(1, 0) - 1(0, 1)$)

Species	Rest Freq. (MHz)	$\int T_R d\nu$ (mK km s ⁻¹)		Ratios This: Gong
		This Work	Gong et al. (2015)	
HC ₇ N	18047.9697	6907(823)	5958(438)	1 : (0.863 ± 0.121)
SiS	18154.8880	64710(1799)	60051(925)	1 : (0.928 ± 0.029)
HC ₃ N	18196.2260	42600(812)	38309(458)	1 : (0.899 ± 0.020)
c-C ₃ H ₂	18343.1430	4784(647)	10904(425)	1 : (2.279 ± 0.321)

Table 6. The abundance ratios (HC₃N: HC₅N: HC₇N: HC₉N) of this work, Gong et al. (2015) and Kawaguchi et al. (1995)

Species	HC ₃ N	HC ₅ N	HC ₇ N	HC ₉ N
This work	100	(28.2±5.0)	(32.0±4.9)	(3.0±0.8)
Gong et al. (2015)	100	(32.9±4.9)	(26.4±4.7)	(1.8±1.0)
Kawaguchi et al. (1995)	100	(15.9±1.2)	(8.9±0.4)	(1.6±0.5)

effect of the variability on the integrated intensity. Therefore, it is assumed that the periodic variations of the stellar IR flux do not modulate molecular line emission here.

The source sizes of HC_{2n+1}N assumed in Kawaguchi et al. (1995) are the same with those in this paper and Gong et al. (2015). The column densities of HC_{2n+1}N among this paper, Gong et al. (2015) and Kawaguchi et al. (1995) in Table 3 can be compared directly, shown in Figure 4. The column densities of HC₃N, HC₅N, HC₇N and HC₉N in this work are greater than the densities derived from Gong et al. (2015) and Kawaguchi et al. (1995). The abundance ratios for HC₃N: HC₅N: HC₇N: HC₉N are shown in Table 6. The ratio in this work is consistent with the ratio derived from Gong et al. (2015), but is greater than the ratio in Kawaguchi et al. (1995). The abundance ratio for C₆H ²Π_{3/2}: C₈H ²Π_{3/2} is calculated to be (1.1 ± 0.3) : 1, which is much smaller than the ratio observed in Gong et al. (2015), (11.9 ± 2.3) : 1. The obvious difference in abundances may suffer from low data quality in lines of C₆H and C₈H.

The transitions of HC₃N and its ¹³C substitutions are optically thin. Thus, the isotopic ratio can be directly obtained from their integrated intensity ratio. The derived ¹²C/¹³C ratios are 32 ± 16 from [HCCCN]/[H¹³CCCN] ($\nu = 0, J = 2 - 1$). This is much smaller than 71 obtained from [¹²CO]/[¹³CO] by Ramstedt & Olofsson (2014) and is also smaller than 49 ± 9 derived from HC₅N and its ¹³C isotopologues by Gong et al. (2015). This value agrees with 34.7 ± 4.3 derived from [SiCC]/[Si¹³CC] by He et al. (2008). Since, there is only one transition used for calculating the isotopic ratio in this work, more transitions need to be adapted as the complementary to derive the isotopic ratio more precisely.

Bell et al. (1992) have reported that the HC₅N molecule in the circumstellar envelope of IRC +10216 traces two molecular regions: a warm one ($T_{ex} \sim 25$ K) traced by high-J transitions, i.e., those with upper-state energies E_U/k greater than 20 K, and a cold region with $T_{ex} \sim 13$ K traced by low-J transitions with $E_U/k < 10$ K. In Figure 5, the rotational temperatures of HC₅N are estimated to be This: Gong: Kawaguchi = 1: 2.1: 5.9. The fitted rotational temperature of HC₅N for high-J transitions is greater. And the rotational temperatures (T_{rot}) of HC₇N and HC₉N are estimated to be This: Gong: Kawaguchi = 1: 2.8: 7.2 and 1: 1.9: 3.3. Similar as in the HC₅N case, the rotational temperatures of HC₇N and HC₉N for high-J transitions are also greater. Therefore, the high-J transitions of the HC₅N, HC₇N and HC₉N molecules in the circumstellar envelope of IRC +10216 trace the warmer molecular regions. The abundance ratios of HC₅N, HC₇N and HC₉N derived from surveys of different frequency ranges are estimated to be This: Gong: Kawaguchi = 100: 43: 55, 100: 24: 28 and 100: 30: 44, respectively. Obvious differences exist in the abundance ratios derived from different transitions, and this result may suffer from opacity effects. It also suggests that the assumption of thermal equilibrium is not accurate to estimate rotational temperatures and column densities.

5. Summary

A spectral line survey of IRC +10216 between 13.3 and 18.5 GHz is carried out using the TMRT. Forty-one spectral lines of 12 different molecules and radicals are detected in total. Several carbon-chain molecules are detected, including HC₃N, HC₅N, HC₇N, HC₉N, C₆H, C₈H, C₆H⁻, l-C₅H, SiC₂, SiC₄ and c-C₃H₂.

The rotational temperatures and column densities of the detected molecules are derived by assuming LTE. Their rotational temperatures range from 4.7 to 40.1 K, and molecular column densities range from 10¹² to 10¹⁵ cm². Molecular abundances relative

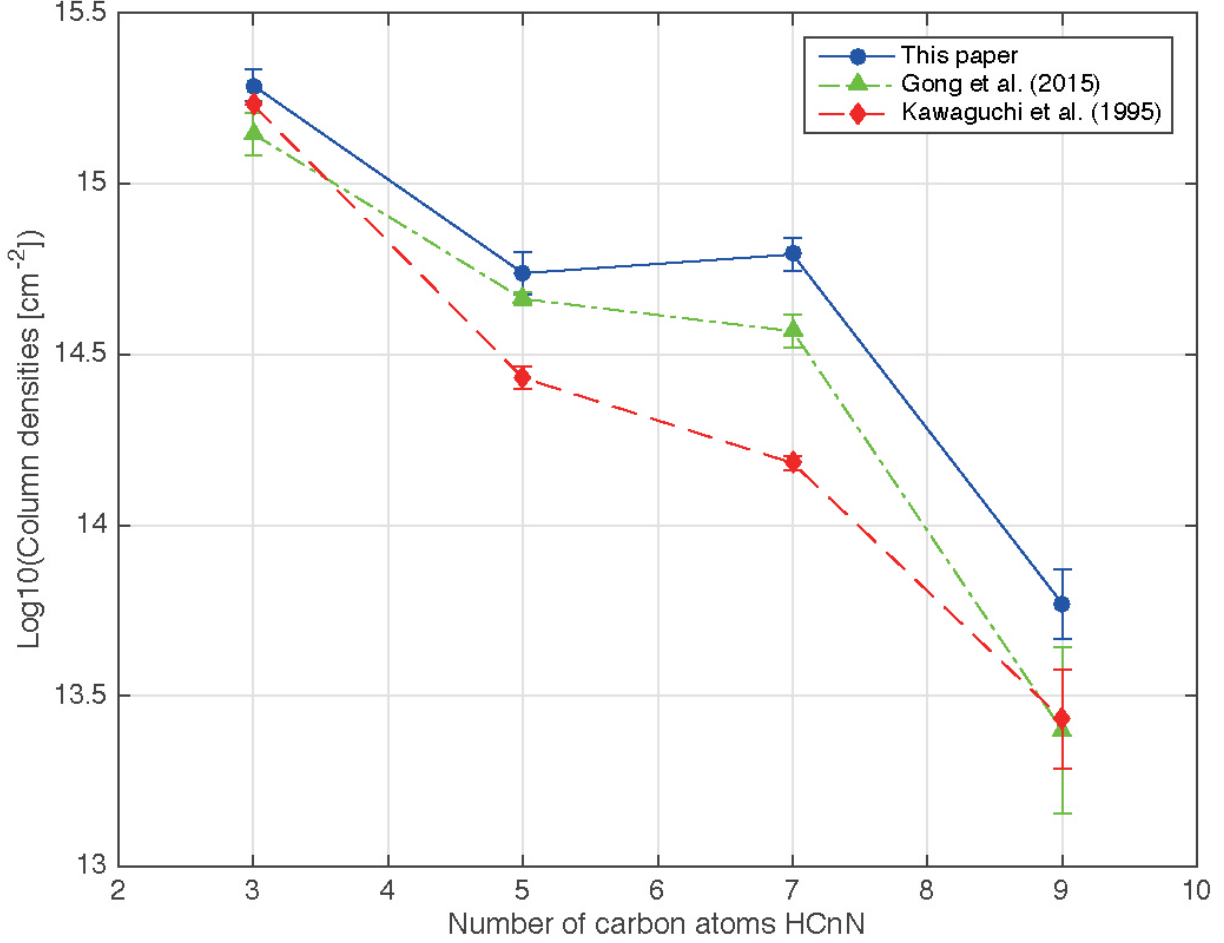


Fig. 4. Comparison of the column densities. The circles with error bars are from our TMRT-65 m observations. The triangles with error bars are obtained from Gong et al. (2015). The asterisks without error bars are obtained from Kawaguchi et al. (1995).

to H₂ range between 2.91×10^{-9} and 9.24×10^{-7} . From the comparison with previous works, it is clear that the higher-J transitions of the HC₅N, HC₇N and HC₉N molecules in the circumstellar envelope of IRC +10216 traces the warmer molecular regions. And there are obvious differences in the abundance ratios derived from different transitions.

Acknowledgements. This work is supported by the Natural Science Foundation of China (No. 11421303, 11590782).

References

- Agúndez, M., Cernicharo, J., & Guélin, M. 2007, *Astrophysical Journal*, 662, L91
 Agúndez, M., Cernicharo, J., & Guélin, M. 2014, *Astronomy & Astrophysics*, 570, A45
 Agúndez, M., Cernicharo, J., Pardo, J. R., Guélin, M., & Phillips, T. G. 2008a, *Astronomy & Astrophysics*, 485, L33
 Agúndez, M., Cernicharo, J., Quintana-Lacaci, G., et al. 2017, *Astronomy & Astrophysics*, 601, Accepted
 Agúndez, M., Fonfría, J., Cernicharo, J., et al. 2012, *Astronomy & Astrophysics*, 543, A48
 Agúndez, M., Fonfría, J. P., Cernicharo, J., Pardo, J. R., & Guélin, M. 2008b, *Astronomy & Astrophysics*, 479, 493
 Araya, E., Hofner, P., Goldsmith, P., Slysh, S., & Takano, S. 2003, *The Astrophysical Journal*, 596, 556
 Avery, L., Amano, T., Bell, M., et al. 1992, *The Astrophysical Journal Supplement Series*, 83, 363
 Bell, M., Feldman, P., & Avery, L. 1992, *The Astrophysical Journal*, 396, 643
 Bell, M. B. 1993, *The Astrophysical Journal*, 417, 305
 Cabezas, C., Cernicharo, J., Alonso, J. L., et al. 2013, *Astrophysical Journal*, 775, 133
 Cernicharo, J., Agúndez, M., Kahane, C., et al. 2011, *Astronomy & Astrophysics*, 529, L3
 Cernicharo, J., Daniel, F., Castro-carrizo, A., et al. 2013, *Astrophysical Journal*, 778, 48
 Cernicharo, J. & Guélin, M. 1987, *Astronomy and Astrophysics*, 183, L10
 Cernicharo, J. & Guélin, M. 1996, *Astronomy and Astrophysics*, 309, L27
 Cernicharo, J., Guélin, M., Agúndez, M., et al. 2007, *Astronomy & Astrophysics*, 467, L37
 Cernicharo, J., Guélin, M., & Kahane, C. 2000, *Astronomy and Astrophysics Supplement Series*, 142, 181
 Cernicharo, J., Guélin, M., M., A., C., M. M., & P., T. 2008, *Astrophysical Journal*, 688, L83
 Cernicharo, J., Marcelino, N., Agúndez, M., & Guélin, M. 2015a, *Astronomy & Astrophysics*, 575, A91
 Cernicharo, J., McCarthy, M. C., Gottlieb, C. A., et al. 2015b, *Astrophysical Journal Letters*, 806, L3

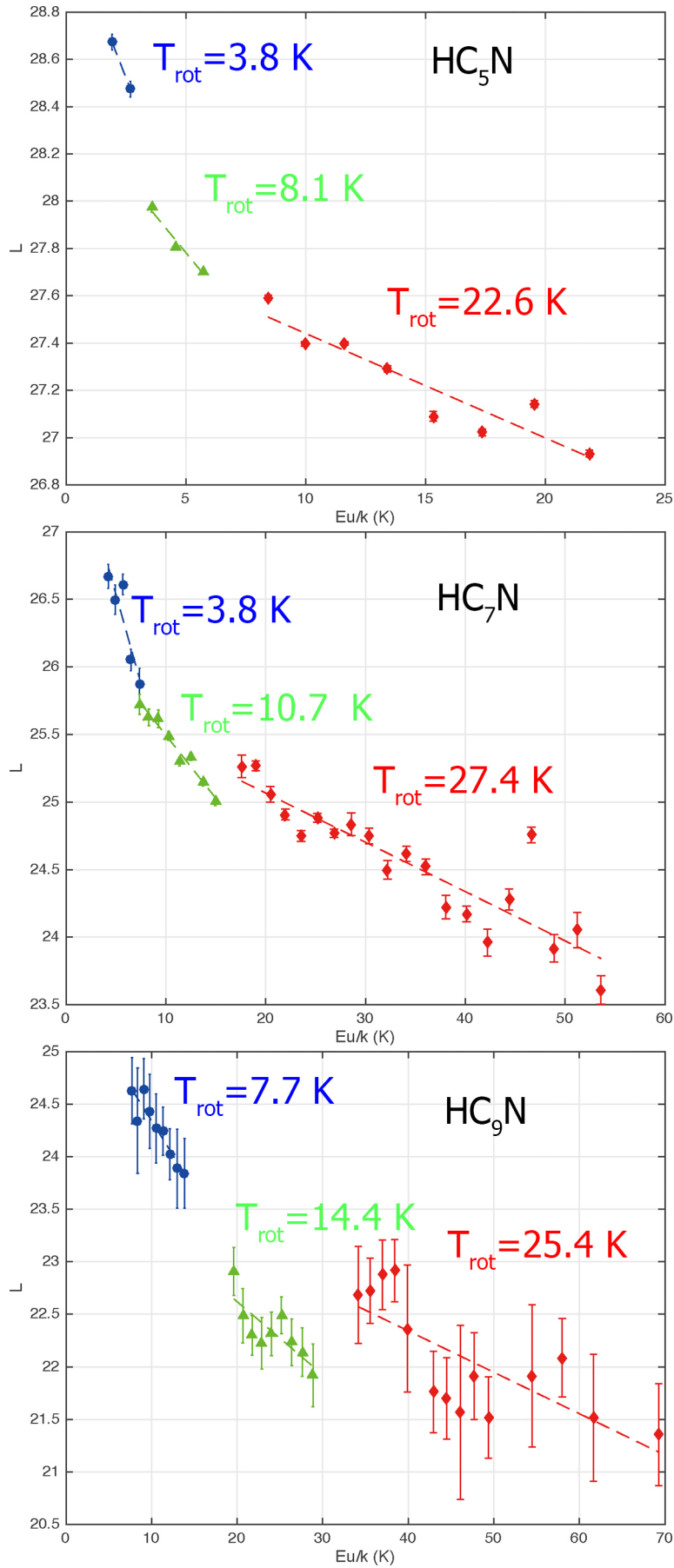


Fig. 5. The red circles are from our TMRT-65 m observations. The green triangles are obtained from Gong et al. (2015). The blue asterisks are obtained from Kawaguchi et al. (1995). The dashed lines of different colors represent linear least-squares fit to the rotational diagram accounting for data obtained from corresponding surveys.

Cernicharo, J., Teyssier, D., Quintana-Lacaci, G., et al. 2014, *Astrophysical Journal Letters*, 796, L21

Cernicharo, J., Waters, L., Decin, L., et al. 2010, *Astronomy & Astrophysics*, 521, L8

Crosas, M. & Menten, K. M. 1997, *The Astrophysical Journal*, 483, 913

Cummins, S. E., Linke, R., & Thaddeus, P. 1986, *The Astrophysical Journal Supplement Series*, 60, 819

De Beck, E., Lombaert, R., Agúndez, M., et al. 2012, *Astronomy & Astrophysics*, 539, 108

Fonfría, J. P., Cernicharo, J., Richter, M. J., & Lacy, J. H. 2008, *The Astrophysical Journal*, 673, 445

Fonfría, J. P., Fernández-López, M., Agúndez, M., et al. 2014, *Monthly Notices of the Royal Astronomical Society*, 445, 3289

Gong, Y., Henkel, C., Spezzano, S., et al. 2015, *Astronomy & Astrophysics*, 574, A56

Groenewegen, M., Barlow, M., Blommaert, J., et al. 2012, *Astronomy & Astrophysics*, 543, L8

Groesbeck, T., Phillips, T., & Blake, G. A. 1994, *The Astrophysical Journal Supplement Series*, 94, 147

Guélin, M., Cernicharo, J., Travers, M., et al. 1997, *Astronomy and Astrophysics*, 317, L1

Guélin, M., Lucas, R., & Cernicharo, J. 1993, *Astronomy and Astrophysics*, 280, L19

Guélin, M., Muller, S., Cernicharo, J., et al. 2000, *Astronomy & Astrophysics*, 363, L9

Guélin, M., Muller, S., Cernicharo, J., McCarthy, M. C., & Thaddeus, P. 2004, *Astronomy & Astrophysics*, 426, L49

He, J., Kwok, S., Müller, H., et al. 2008, *The Astrophysical Journal Supplement Series*, 177, 275

Henkel, C., Matthews, H., & Morris, M. 1983, *The Astrophysical Journal*, 267, 184

Henning, T. & Salama, F. 1998, *Science*, 282, 2204

Johansson, L., Andersson, C., Elder, J., et al. 1985, *Astronomy and Astrophysics Supplement Series*, 60, 135

Johansson, L. E., Andersson, C., Elder, J., et al. 1984, *Astronomy and Astrophysics*, 130, 227

Kahane, C., Gomez-Gonzalez, J., Cernicharo, J., & Guélin, M. 1988, *Astronomy and Astrophysics*, 190, 167

Kawaguchi, K., Kasai, Y., Ishikawa, S.-I., & Kaifu, N. 1995, *Publications of the Astronomical Society of Japan*, 47, 853

Li, J., Shen, Z.-Q., Wang, J., et al. 2016, *The Astrophysical Journal*, 824, 136

Lovas, F. J. 2004, *Journal of Physical and Chemical Reference Data*, 33, 177

Lucas, R., Guélin, M., Kahane, C., Audinos, P., & Cernicharo, J. 1995, *Astrophysics and Space Science*, 224, 293

Men'shchikov, A. B., Balega, Y., Bloecker, T., Osterbart, R., & Weigelt, G. 2001, *Astronomy & Astrophysics*, 368, 497

Müller, H. S., Schlöder, F., Stutzki, J., & Winnewisser, G. 2005, *Journal of Molecular Structure*, 742, 215

Olofsson, H., Johansson, L. E. B., Hjalmarsen, A., & NguyenQuangRieu. 1982, *Astronomy & Astrophysics*, 107, 128

Patel, N. A., Young, K. H., Gottlieb, C. A., et al. 2011, *The Astrophysical Journal Supplement Series*, 193, 17

Pickett, H., Poynter, R., Cohen, E., et al. 1998, *Journal of Quantitative Spectroscopy and Radiative Transfer*, 60, 883

Pulliam, R. L., Savage, C., Agúndez, M., et al. 2010, *Astrophysical Journal Letters*, 725, L181

Quintana-Lacaci, G., Cernicharo, J., Agúndez, M., et al. 2016, *Astrophysical Journal*, 818, 192

Ramstedt, S. & Olofsson, H. 2014, *Astronomy and Astrophysics*, 566, 15

Remijan, A. J., Hollis, J., Lovas, F., et al. 2007, *The Astrophysical Journal Letters*, 664, L47

Sakai, N., Saruwatari, O., Sakai, T., Takano, S., & Yamamoto, S. 2010, *Astronomy & Astrophysics*, 512, A31

Tenenbaum, E. D., Dodd, J. L., Milam, S. N., Woolf, N. J., & Ziurys, L. M. 2010, *Astrophysical Journal Supplement*, 190, 348

Thaddeus, P., Cummins, S. E., & Linke, R. A. 1984, 283, 145

Tielens, A. G. 2008, *Annu. Rev. Astron. Astrophys.*, 46, 289

Velilla Prieto, L., Cernicharo, J., Quintana-Lacaci, G., et al. 2015, *Astrophysical Journal Letters*, 805, L13

Winnewisser, G. & Walmsley, C. 1978, *Astronomy and Astrophysics*, 70, L37

Yan, Z., Shen, Z.-Q., Wu, X.-J., et al. 2015, *The Astrophysical Journal*, 814, 5

Zack, L. N., Halfen, D. T., & Ziurys, L. M. 2011, *Astrophysical Journal Letters*, 733, L36

Ziurys, L. M., Apponi, A. J., Guélin, M., & Cernicharo, J. 1995, *Astrophysical Journal*, 445, L47

Ziurys, L. M., Savage, C., Highberger, J., et al. 2002, *The Astrophysical Journal Letters*, 564, L45

Table 2. Line Parameters of Transitions Detected in IRC +10216.

(1)	(2)	(3)	(4)	(5)	(6)	(7)	(8)	(9)	(10)	(11)	
Species	Transitions	Rest Freq. (MHz)	E_u/k (K)	Observing date	FWHM beam (")	peak intensity (mK)	v_{exp} (km s ⁻¹)	LSR velocity (km s ⁻¹)	$\int T_{MB} dv$ (mK km s ⁻¹)	Notes	
HC ₃ N	$\nu = 0, J = 2 - 1$	18196.2260	1.30994	2016Apr10	53	504.3(6.8)	13.7(1.5)	-26.2(1.5)	10337(197)	D	
	$\nu = 0, J = 2 - 1$	17633.7460	1.26928	2016Apr10	55	27.2(5.4)	13.1(1.6)	-27.1(1.6)	306(157)	D	
	$\nu = 0, J = 2 - 1$	18119.0430	1.30437	2016Apr10	54						
	$\nu = 0, J = 2 - 1$	18120.7670	1.30445	2016Apr10	54	24.3(3.3)			711(96)	B,S	
HC ₅ N	$\nu = 0, J = 5 - 4$	13313.3119	1.91685	2016Apr10	73	128.9(3.5)	15.5(2.1)	-27.4(2.1)	3063(102)	F	
	$\nu = 0, J = 6 - 5$	15975.9663	2.68359	2016Mar25	61	203.7(5.5)	14.5(1.7)	-26.2(1.7)	4870(160)	F	
HC ₇ N	$\nu = 0, J = 12 - 11$	13535.9990	4.22252	2016Apr10	72	52.6(3.9)	15.2(2.0)	-26.3(2.0)	1279(113)	F	
	$\nu = 0, J = 13 - 12$	14663.9936	4.92625	2016Mar25	66	64.7(5.4)	14.0(1.9)	-26.4(1.9)	1463(157)	F	
	$\nu = 0, J = 14 - 13$	15791.9870	5.68424	2016Mar25	61	94.8(5.7)	14.8(1.7)	-25.6(1.7)	2163(165)	F	
	$\nu = 0, J = 15 - 14$	16919.9791	6.49617	2016Mar10	57	74.5(4.4)	13.6(1.6)	-26.1(1.6)	1578(128)	D	
	$\nu = 0, J = 16 - 15$	18047.9697	7.36235	2016Apr10	54	82.6(6.7)	13.6(1.5)	-26.0(1.5)	1629(194)	D	
		$\nu = 0, J = 23 - 22$	13363.8008	7.69636	2016Apr10	73	20.0(3.9)	13.4(2.1)	-26.3(2.1)	357(113)	F
HC ₉ N	$\nu = 0, J = 24 - 23$	13944.8317	8.36550	2016Mar25	70	22.9(5.4)	14.8(2.0)	-26.2(2.0)	314(157)	F	
	$\nu = 0, J = 25 - 24$	14525.8622	9.06270	2016Mar25	67	23.4(4.9)	14.3(1.9)	-26.2(1.9)	496(142)	F	
	$\nu = 0, J = 26 - 25$	15106.8921	9.78767	2016Mar25	64	23.0(5.7)	13.7(1.8)	-26.9(1.8)	468(165)	F	
	$\nu = 0, J = 27 - 26$	15687.9215	10.54055	2016Mar25	62	28.6(5.1)	13.1(1.8)	-27.1(1.8)	451(148)	F	
	$\nu = 0, J = 28 - 27$	16268.9503	11.32135	2016Mar10	60	23.4(3.9)	12.8(1.7)	-28.4(1.7)	498(113)	D	
	$\nu = 0, J = 29 - 28$	16849.9786	12.13005	2016Mar10	58	24.6(3.8)	13.9(1.6)	-26.3(1.6)	453(110)	F	
	$\nu = 0, J = 30 - 29$	17431.0062	12.96652	2016Apr10	56	33.5(5.8)	13.0(1.6)	-27.0(1.6)	447(168)	D	
	$\nu = 0, J = 31 - 30$	18012.0333	13.83105	2016Apr10	54	24.7(5.5)	14.4(1.5)	-27.2(1.5)	483(160)	D	
		$\nu = 0, J = 1(1,0) - 1(0,1)$	18343.1430	3.23012	2016Apr10	53	53.8(6.1)	14.8(1.5)	-26.3(1.5)	1161(157)	D
		$J = 7/2 - 5/2, F = 4 - 3, l = e$	16706.6928	1.71872	2016Mar16	58					
1-C ₅ H ² Π _{1/2}	$J = 7/2 - 5/2, F = 3 - 2, l = e$	16707.5764	1.71876	2016Mar16	58	13.4(3.1)			314(90)	B,S	
	$J = 7/2 - 5/2, F = 3 - 3, l = e$	16708.6662	1.71881	2016Mar16	58						
	$J = 7/2 - 5/2, F = 4 - 3, l = f$	16710.5921	1.71962	2016Mar16	58						
	$J = 7/2 - 5/2, F = 3 - 2, l = f$	16711.6058	1.71924	2016Mar16	58	11.1(3.1)			313(90)	B,S	
		$J = 6 - 5$	16522.3290	2.77528	2016Mar16	59	14.6(4.0)	15.7(3.3)	-28.7(3.3)	345(116)	D,S
C ₆ H ⁻	$J = 11/2 - 9/2, l = f$	15343.1726	24.51330	2016Mar25	63	20.9(5.3)	14.3(1.8)	-27.7(1.8)	291(154)	F	
	$J = 11/2 - 9/2, l = e$	15371.5462	24.52142	2016Mar25	63	12.1(3.8)	14.4(3.6)	-26.0(3.6)	272(110)	F,S	
	$J = 13/2 - 11/2, l = f$	18135.2758	25.38366	2016Apr10	54	16.1(3.6)	10.6(3.0)	-26.4(3.0)	275(104)	F,S	
	$J = 13/2 - 11/2, l = e$	18163.8788	25.39309	2016Apr10	53	25.3(5.4)	13.7(1.5)	-26.6(1.5)	264(157)	D	
C ₆ H ² Π _{3/2}	$J = 11/2 - 9/2, l = e$	15248.2791	2.12884	2016Mar25	64	33.2(5.3)			704(154)	B	
	$J = 11/2 - 9/2, l = f$	15249.1203	2.12903	2016Mar25	64						
	$J = 13/2 - 11/2, l = e$	18020.6059	2.99379	2016Apr10	54	24.4(6.7)			576(194)	B	
	$J = 13/2 - 11/2, l = f$	18021.7828	2.99385	2016Apr10	54						
C ₈ H ² Π _{3/2}	$J = 27/2 - 25/2$	15840.0020	5.40584	2016Mar25	61	14.8(3.7)	10.6(3.5)	-29.1(3.5)	277(107)	F,S	
	$J = 29/2 - 27/2$	17013.3256	6.22239	2016Mar16	57	17.1(3.6)	15.4(3.2)	-25.0(3.2)	276(104)	F,S	
	$J = 31/2 - 29/2$	18186.6470	7.09520	2016Mar16	53	15.8(5.1)	15.0(3.0)	-26.4(3.0)	254(148)	F,S	
SiS	$\nu = 0, J = 1 - 0$	18154.8880	0.87129	2016Apr10	53	480.6(6.4)	14.2(1.5)	-26.2(1.5)	6692(186)	D	
	$\nu = 0, J = 7(2,5) - 7(2,6)$	15697.7396	40.16052	2016Mar25	62	22.3(5.6)	12.2(1.7)	-25.6(1.7)	350(162)	F	
	$J = 5 - 4$	15337.6950	2.20824	2016Mar25	63	22.3(5.3)	14.3(1.8)	-27.4(1.8)	400(154)	F	

Notes. The numbers in parentheses represent the 1σ errors. The rms noise of peak intensity is estimated from frequency ranges around each particular transition where the spectrum is apparently free of lines. The error for expansion velocity and LSR velocity is the velocity width of a channel. And the error of integrated intensity given here is the product of the rms noise of peak intensity and the width of the line for about 29 km s^{-1} . Each column represents the following information, Col. (1): molecule name; Col. (2): transition; Col. (3): rest frequency; Col. (4): E_U/k , the upper level energy in K; Col. (5): observing date; Col. (6): FWHM beam; Col. (7): peak intensity of main beam temperature; Col. (8): expansion velocity; Col. (9): LSR velocity; Col. (10): integrated intensity. (D) The lines fitted with double peaked profiles are marked with "D". (F) The lines fitted with flat-topped profiles are marked with "F". (B) The blended transitions are marked with "B". (S) Transitions that are smoothed to improve signal to noise ratio are marked with "S".